High-numerical-aperture effects in photoresist

Donis G. Flagello and Tom D. Milster

Two-beam and three-beam vector interference in thin photoresist films is used to illustrate the striking differences between s-polarized and p-polarized high-numerical-aperture illumination. Both simulations and experiments are performed for several cases, including undyed photoresist on silicon, dyed photoresist on silicon, and the addition of an antireflective layer between the photoresist and the silicon. A 0.85 numerical-aperture system is examined. The major differences between s- and p-polarized illumination include elliptical versus rectangular features and lower contrast for p-polarized images. © 1997 Optical Society of America

1. Introduction

The development of large-field and high-numerical-aperture (NA) lenses is most evident in the microelectronics industry, where the demand for increased resolution constantly pushes state-of-the-art lens manufacturing technology. Current photolithographic systems have $0.5 < \text{NA} < 0.7$.[1] These systems reimage mask patterns into photoresist layers with reduction ratios between 1 and 5. Because of strict linewidth control requirements, it is essential to understand imaging within the photoresist film because of large marginal ray angles. In this paper we discuss several experimentally observed effects from large oblique angles of incidence.

For periodic objects, the simplest realization of photolithographic systems is either two-beam or three-beam interference. Two-beam interference is useful to describe systems that limit the 0th order, as in alternating phase masks.[2] Three-beam interference is useful for describing classical systems. In our research we use an experimental setup that approximates the output of a 0.85 NA reduction stepper used at the limits of its resolution. The experimental setup includes a periodic grating mask to obtain diffracted orders and mirrors that simulate the imaging lens, which results in the desired two-beam and

three-beam interference inside a photoresist thin film. We also present a theory based on a plane-wave decomposition of the vector image field.

In the following sections we describe the theory, experiment, and results of our investigation. In Section 2 we discuss a vector theory that defines the image distribution with a Joule's heat term instead of the traditional Poynting vector. Both two-beam and three-beam analyses are applied to images inside the photoresist film. In Section 3 we describe the experimental setup and a unique decoration technique used to obtain information about the recorded image. In Section 4 we present our results for the two-beam and three-beam experiments. Our conclusions are summarized in Section 5.

2. Theory

In this section we briefly outline the formalism of two-beam and three-beam vector imaging theory. Details of the derivation can be found in Refs. 2–4. Only the relevant details are presented here.

A. Energy and the Image Distribution

Traditionally, the magnitude of the time-average Poynting vector is used to calculate image irradiance $I = |\langle \mathbf{S} \rangle|$. However, it is more appropriate to examine the absorbed energy in a volume when one calculates the image field within a thin film of photoresist. The absorbed energy can be calculated by considering the conservation of energy with use of Poynting's theorem. The absorbed energy Q is given by the divergence of the real part of the Poynting vector:

$$Q = k_0 \mathfrak{I} n \kappa |\mathbf{E}|^2, \tag{1}$$

where $k_0 = 2\pi/\lambda_0$. λ_0 is the free-space wavelength, n and κ are the real and imaginary parts of the re-
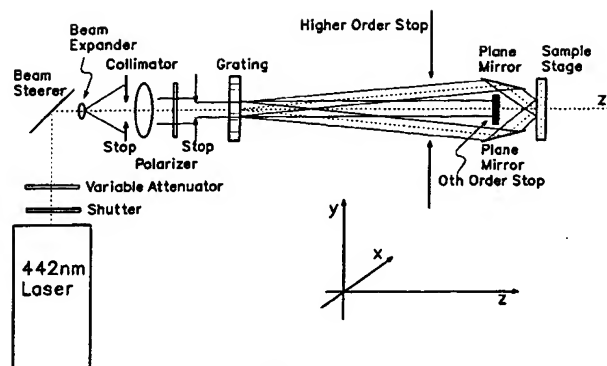
Fig. 1. Experimental setup.

fractive index $N = n - i\kappa$, $\mathfrak{Y} = 2.655 \times 10^{-3}$ Ω is the optical admittance of free space, and Q represents the form of the recorded image distribution within an absorbing medium, which is interpreted as the mean energy absorbed per unit volume per second in units of power per unit volume. Any direct investigation into the structure of the image, such as a physical recording into a photosensitive film, is proportional to $|\mathbf{E}|^2$.

The physical measurement of the irradiance in air of a normally incident plane wave is related to $|\mathbf{E}|$ by

$$I = |\langle \mathbf{S} \rangle| = \frac{1}{2} \mathfrak{Y} |\mathbf{E}|^2, \qquad (2)$$

which yields

$$|\mathbf{E}| = \sqrt{\frac{2I}{\mathfrak{Y}}}. \qquad (3)$$

Equation (3) is used in verification experiments to link theory to physical measurements. **E** is given in units of millivolts per centimeter, I in units of milliwatts per square centimeter, and Q in units of milliwatts per cubic centimeter.

B. Vector Two-Beam and Three-Beam Theories

References 2–4 show that high NA imaging in photoresist films can be modeled by a Debye plane-wave decomposition of the electric fields. Because the image can be considered as a summation of plane waves, the simplest form of this theory reduces to two-beam and three-beam vector interference. This simplification results in concise analytic solutions of the energy distribution within a film.

The electric-field distribution in the pupil of the imaging lens is a function of the mask pattern and the illumination conditions. If the mask pattern is a 50% duty cycle grating at the limit of coherent resolution for the lens, only the ± 1 and 0 diffracted orders are transmitted through the system. If the grating is chrome on glass, the ± 1 orders have an amplitude $2/\pi$ lower than the zero order. Application of a 180° alternating phase-shifted mask removes the zero order.

The experimental setup is shown in Fig. 1. The optical setup mimics a standard coherent projector with the main exception that the imaging lens is replaced by two mirrors. Hence the ± 1st orders are reflected from the mirrors and combined at the image plane where a photoresist thin-film stack is placed. The z axis is normal to the film stack. The grating mask is illuminated with polarized, collimated illumination. The angular separation 2θ of the ± 1st orders on the mask side is small so that $\cos\theta \approx 1$. Because the beam diameter is preserved from mask to image side there is no significant obliquity factor. Wave-front aberrations, except for focus in the three-beam application, are negligible and are not considered here.

If the mask grating lines are parallel to the x axis, x-polarized illumination is s polarized at the film assembly. With y-polarized illumination, the field is p polarized at the film assembly. The symmetric orders reflect from the mirrors with an angular separation of $2\theta'$. The incident medium is air with $N_i = 1$. Direction cosine relationships with this geometry are

$$\beta' = \sin\theta',$$
$$\gamma' = \cos\theta',$$
$$\gamma' = \sqrt{1 - \beta'^2}. \qquad (4)$$

It can be shown that components of the total two-beam electric field in the top layer of the film stack for s polarization are

$$E_y(y; z) = E_z(y; z) = 0,$$
$$E_x(y; z) = c_1 \cos(2\pi y \beta') [F(\beta'; z)]_s, \qquad (5)$$

where

$$[F(\beta'; z)]_s = \frac{\tau_s}{\tau_{\mathrm{II}s}} [\exp(i\phi) + r_{\mathrm{II}s} \exp(-i\phi)]; \qquad (6)$$

$$\phi = 2\pi N_1 (d - z + z_0)\gamma_1; \qquad (7)$$

$$c_1 = 2a_0 \exp(-i2\pi\gamma' z_0); \qquad (8)$$

d is the photoresist thickness; z_0 is the absolute position of the 1st film interface (between the air and the photoresist film) referenced to the Gaussian focus in air, as shown in Fig. 2; z is the relative position of the observation plane within the photoresist film, such that it ranges from z_0 at the 1st interface to $z_0 + d$ at the bottom of the photoresist; γ_1 is the z-direction cosine in the photoresist; c_1 represents the constant amplitude and phase of the incident plane waves; and a_0 is an amplitude term generated from the object transform and is a function of the initial electric-field amplitude illuminating the object. We generated the factor of 2 from summing two plane waves into a cosine term. τ, τ_{II}, and r_{II} are complex amplitude transmission and reflection coefficients as defined in Ref. 3. τ is the transmission coefficient for the full thin-film stack. τ_{II} and r_{II} refer to the transmission and reflection coefficients from interface II. N_1 is
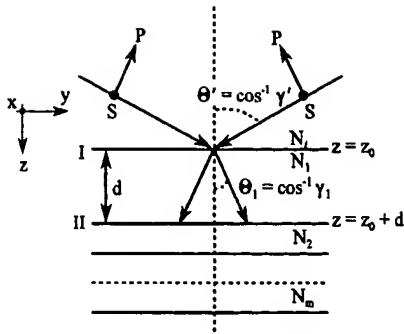
Fig. 2. Propagation vectors incident on film assembly for two-beam interference.

the complex refractive index of the photoresist. The field is constant along x, so no x dependence is indicated. All x, y, and z dimensions are normalized to the vacuum wavelength λ_0.

Calculation of the image distribution for two-beam s-polarized illumination yields

$$Q_s(y; z) = k_0 \mathfrak{I} n \kappa |\mathbf{E}_s(y; z)|^2$$
$$= k_0 \mathfrak{I} n \kappa |c_1|^2 |[F(\beta'; z)_s]|^2 \cos^2(2\pi y \beta'). \quad (9)$$

In the absence of a film, $[F(\beta'; z)]_s = 1$, and Eq. (9) is proportional to the classic two-beam interference equation, i.e., $Q_s \sim \cos^2(2\pi y \beta')$.

The component fields for two-beam p-polarized illumination are

$$E_x(y; z) = 0,$$
$$E_y(y; z) = c_1 \gamma' [F(\beta'; z)]_{yP} \cos(2\pi y \beta'),$$
$$E_z(y; z) = c_1 i \beta' [F(\beta'; z)]_{zP} \sin(2\pi y \beta'), \quad (10)$$

where

$$[F(\beta'; z)]_{yP} = \frac{\tau_p}{\tau_{IIP}} [\exp(i\phi) + r_{IIP} \exp(-i\phi)], \quad (11)$$

$$[F(\beta'; z)]_{zP} = \frac{\tau_p \gamma'}{\tau_{IIP} n \gamma_1} [\exp(i\phi) - r_{IIP} \exp(-i\phi)]. \quad (12)$$

The image distribution is

$$Q_P(y; z) = k_0 \mathfrak{I} n \kappa [|E_y(y; z)|^2 + |E_z(y; z)|^2]$$
$$= k_0 \mathfrak{I} n \kappa |c_1|^2 \{|[F(\beta'; z)]_{yP}|^2 \gamma'^2 \cos^2(2\pi y \beta')$$
$$+ |[F(\beta'; z)]_{zP}|^2 \beta'^2 \sin^2(2\pi y \beta')\}. \quad (13)$$

Equation (11) indicates the presence of z-component fringes that beat $180°$ out of phase with the y-component fringes. The magnitude of the z image scales quadratically with obliquity. In both s and p cases the initial phase terms cancel and do not contribute to the image.

The three-beam model builds on the two-beam

model by adding a 0th-order term. The s-polarized image distribution is

$$Q_s(y; z) = k_0 \mathfrak{I} n \kappa |\{c_1 [F(0; z)]_s$$
$$+ c_2 [F(\beta'; z)]_s \cos(2\pi y \beta')\}|^2, \quad (14)$$

where

$$c_1 = a_0 \exp(-i2\pi z_0), \quad c_2 = 2a_1 \exp(-i2\pi \gamma' z_0). \quad (15)$$

a_0 and a_1 are the amplitude terms for the 0th and $\pm$1st orders and the factors c_1 and c_2 contain focus phase terms.

A similar treatment for p polarization results in

$$Q_P(y; z) = k_0 \mathfrak{I} n \kappa \{|c_1 [F(0; z)]_{yP} + c_2 \gamma' [F(\beta'; z)]_{yP}$$
$$\times \cos(2\pi y \beta')|^2 + |c_2 \beta' [F(\beta'; z)]_{zP}$$
$$\times \sin(2\pi y \beta')|^2\}. \quad (16)$$

3. Experimental Technique

With reference to Fig. 1, a 150-mW, 442-nm He–Cd laser is used as the exposing source. The laser beam full width at $1/e^2$ maximum is approximately 1 mm. After passing through an electronic shutter and a variable attenuator, a beam steerer brings it into the rear of a 0.75 NA beam expander with an entrance pupil size of 7 mm. The beamwidth is apertured to a 9-mm diameter at the $f = 120$-mm collimator lens. The light proceeds through a polarizer and is stopped to a 7-mm diameter. The apertured beam illuminates the object, which is a 50% duty cycle chrome grating on glass with a period of 10 µm. The resulting $\pm$1st orders have an object-side NA of 0.022. All orders diffracted from the grating are blocked except for the 0th and $\pm$1st orders. The two-beam configuration has an additional block for the 0th order. The $\pm$1st orders strike mirrors that are placed 1020 mm from the object and spaced 48 mm apart. They are tilted such that the obliquity of the outer orders with the optical axis is $58.2°$ for NA' of 0.85. One can adjust the power of the beams by using the variable neutral density attenuator such that the total power incident on the mask is equal for each polarization.

The experiments rely on an examination of developed cross sections of exposed images in the photoresist. Uetani et al.[5] used a cross-sectioning exposure technique to understand the internal structure of a resist line. They exposed and developed a set of positive photoresist lines. The lines were then cross sectioned and flood exposed from the side. Uetani et al. were concerned with the chemical mechanisms of development. They failed to take into account near-field diffraction that resulted from the side exposure of a 2-µm line. In contrast, La Tulipe et al.[6] developed a decoration technique without the need for a second exposure by choosing the appropriate processing conditions. They analyzed silylated photoresist images for a dry development process. After exposure and a postexposure silylation treatment, the photoresist surface was gold coated. They cross sectioned the surface by cleaving and then developing it
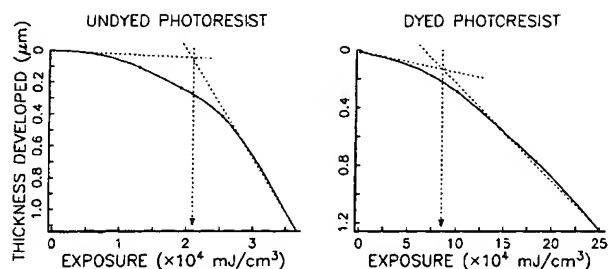
Fig. 3. Characteristic curves of undyed and dyed photoresist.

Step	Process Description
1	Precoat adhesive promoter on substrate and spin dry for 30 s.
2	Spin coat photoresist on desired film/substrate combination; spin dry for 30 s.
3	Postapply bake at 90 °C on a plate for 60 s.
4	Expose photoresist/film stack
5	Sputter approximately 20-Å AuPd on photoresist surface
6	Cross section photoresist by cleaving perpendicular to exposed grating
7	Develop photoresist with Shipley Microposit 351 developer at a dilution of 3 parts deionized water and 2 parts developer at 21 °C for 30 s.
8	Rinse in deionized water and dry
9	Sputter additional 20-Å AuPd on photoresist cross section
10	Analyze under SEM

in an aqueous-based developer. The gold prevented the development of the top photoresist surface. Because the rate of development is different in the silylated and unsilylated regions, the cross sections show highlighted silylated regions. However, the nature of the original image record is altered because of postexposure bake and silylation treatments. The experimental research presented here is based on La Tulipe *et al.*'s decoration technique, but the process is optimized to obtain maximum information from the exposed image. Processes and treatments that alter the recorded image after exposure are avoided.

In our experiments we use a positive photoresist based on traditional diazo-novalac chemistry. A version of this photoresist with an added dye is also used to increase the effect of absorption. Their characteristic curves are shown in Fig. 3 for a development time of 30 s. The thickness of removed photoresist is plotted as a function of average exposure that has been absorbed in the fraction of the removed photoresist. The exposure is defined as $Q \times t$ in units of millijoules per cubic centimeter, where t is the exposure time. Traditionally, the measured irradiance is used instead of Q, but the definition of exposure here gives a form consistent with energy conservation within the volume of a film. It is convenient to define the minimum exposure that will start to develop the photoresist at the inflection point of the curve. This is called the speed point. The curves are nonlinear, but like photographic emulsions, they have a region that is approximately linear.

The two versions of photoresist, undyed and dyed, have a real refractive index of $n = 1.656$ at $\lambda = 0.442$ μm. The undyed photoresist has an unexposed absorption coefficient of 0.18 μm^{-1} and a fully exposed coefficient of 0.05 μm^{-1}. These values correspond to imaginary index coefficients of $\kappa = 0.006$ and $\kappa = 0.002$, respectively. Although the relative change is large, the absolute change in refractive index is small. For simplification, κ is given as the average value of 0.004. We formulated the dyed photoresist by adding 1% by weight of a Kodak 436 dye, which is assumed to be relatively nonphotosensitive. The unexposed and exposed absorption coefficients of the dyed photoresist are $\alpha = 0.55$ μm^{-1} and $\alpha = 0.39$ μm^{-1}, respectively, which correspond to $\kappa = 0.02$ and $\kappa = 0.014$, respectively. Because the difference in κ

is nearly identical to the undyed material, the dye is considered a nonphotoactive species.

Because the dimension of the images are submicrometer, comparisons with the absolute photoresist response can be obscured by large amounts of experimental error that is due to the development process. The speed can often vary as much as $\pm 10\%$ because of variations in developer dilution, develop temperature, postapply bake time, and temperature, as well as any error in the exposure energy measurement. Examination of specific structural detail, rather than absolute dimensional measurements, is relatively insensitive to process fluctuations. The experiment concentrates on a comparison of the relative image structure and unique differences specific to s and p polarization. The theoretical comparisons with experiments assume that the photoresist responds to the image in an approximately linear fashion over a substantial exposure range.

The general experimental process outline is shown in Table 1. For each experiment, scanning electron microscope (SEM) cross-sectional views are compared with simulations of the exposure. The exposure is simulated by use of the characteristic photoresist curves as a simple mapping function for $Q \times t$. This produces isoexposure contours with related plots along various slices. The contour levels used for undyed photoresist simulations are 20, 25, and 30 J/cm^3, whereas for the dyed photoresist they are 100, 150, and 200 J/cm^3. All photoresist and film combinations use silicon as a substrate with a refractive index of $N_s = 4.75 - 0.15i$ at 0.442 μm. The substrates used in these experiments had ~30-Å oxide with an index of 1.48. The simulations use the measured experimental thicknesses and include the minor effect of the native oxide.

4. Results

Table 2 displays combinations of experimental parameters investigated in this study, where I is the measured irradiance of the beams and a_0 is the related electric-field amplitude. N_1 and N_2 are indices for the photoresist and intermediate layers, respec-

Table 2. Experimental Parameters

| Configuration | Film Assembly | | | | Optics | | | | | |
	N_1	N_2	d_1	d_2	I_0 (mW/cm^2)	$I_{\pm 1}$ (mW/cm^2)	a_0 (mV/cm)	$a_{\pm 1}$ (mV/cm)	t (s)	Number of Beams
1	$1.656 - 0.004i$	1.48	1.095	0.003	0.53	—	0.63	—	30, 60	2
2	$1.656 - 0.017i$	1.48	1.25	0.003	0.53	—	0.63	—	75	2
3	$1.656 - 0.004i$	$1.467 - 0.001i$	1.08	0.478	0.53	—	0.63	—	30	2
4	$1.656 - 0.017i$	$2.25 - 0.330i$	1.24	0.525	0.53	—	0.63	—	90	2
5	$1.656 - 0.004i$	1.48	1.19	0.003	1.2	0.43	0.95	0.57	10	3
6	$1.656 - 0.004i$	1.48	1.7	0.003	0.53	0.53	0.63	0.63	15	3

tively. For configurations 1, 2, 5, and 6, the intermediate layer is the native oxide. d_1 and d_2 are the photoresist and intermediate layer thicknesses, respectively. In the following paragraphs we describe detailed results from each configuration.

The objective of configuration 1 is to examine the image distribution within undyed photoresist over a Si substrate with s and p polarizations with use of two-beam interference. Figure 4(a) shows the resultant cross-sectional SEM views for s polarization with two exposure times. Figure 5(a) shows these exposures for the p-polarization case. The dark regions in the photographs are areas that have received greater exposure and have developed faster than the lighter regions. The light regions are raised compared with the dark regions, creating a relief pattern in the exposure. The photoresist/air interface is labeled I and the photoresist/substrate interface is labeled II. These photographs compare well to the simulated isoexposure contours in Fig. 4(b) and Fig. 5(b). The 30-s and 60-s exposures explore the range of the image structure. Low-exposure energies show that the s-polarization features are elliptical in

shape compared with the rectangular shapes for p polarization. The measured periodicity between the interference minima in Figs. 4(a) and 5(a) is 0.248 μm, which corresponds to plane waves at 0.856 NA. With p polarization, the z-axis modulation along interference minima is absent in the 30-s exposure. Analysis of the simulations indicate that the exposure of this modulation is below 20 J/cm^3, which is the speed point of the photoresist. A higher exposure time is required to reveal these patterns. The 60-s exposure in Fig. 5(a) confirms this prediction, showing increased development of resist at intersections of the interference and standing-wave minima. Unfortunately, at this level of exposure, much of the detail is removed and higher-order lateral development effects are observed. For example, between any standing-wave maxima the areas of low exposure are developed at a faster rate than is predicted by the simple development model. The 60-s exposure for s polarization causes extensive development effects that are evidenced by lateral development between standing-wave maxima. Finally, both polarization simulations show the existence of standing-wave nodes at interface II.
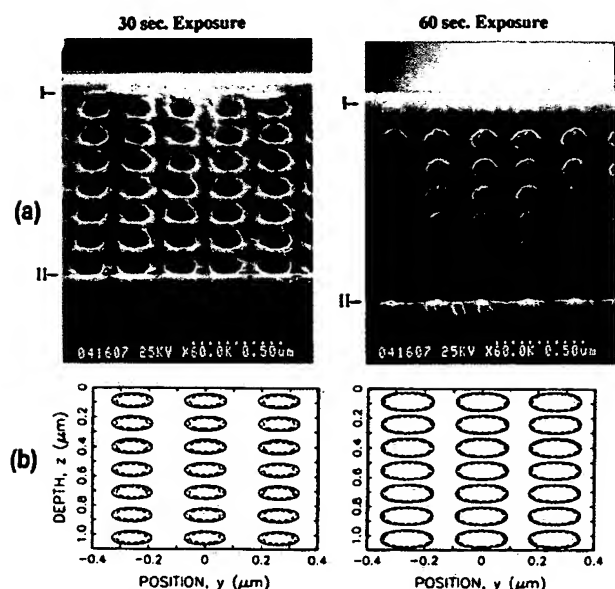

Fig. 4. (a) SEM results for configuration 1: undyed photoresist over Si with s polarization; (b) simulation with isoexposure contours of 20-, 25-, and 30-J/cm^3 levels.
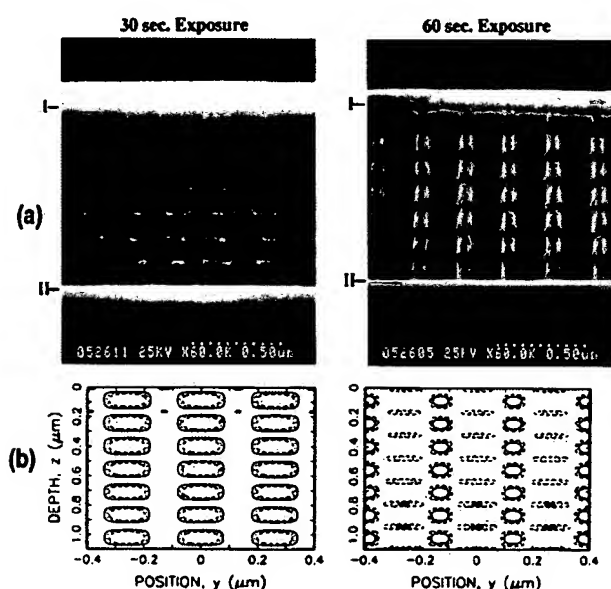

Fig. 5. (a) SEM results for configuration 1: undyed photoresist over Si with p polarization; (b) simulation with isoexposure contours of 20-, 25-, and 30-J/cm^3 levels.
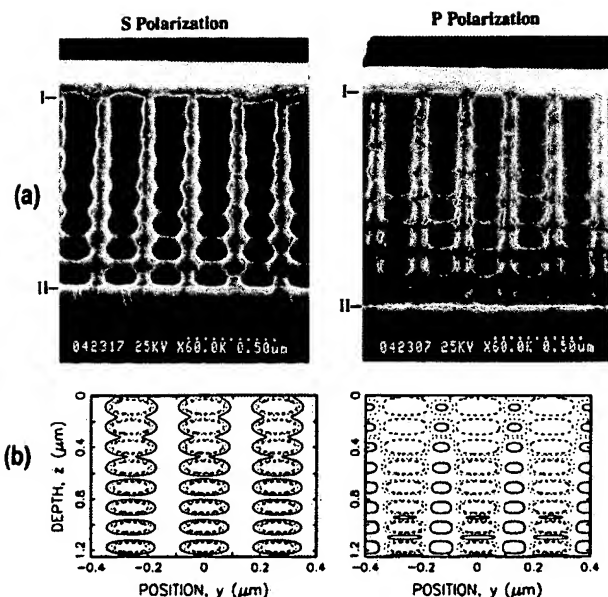
Fig. 6. (a) SEM results for configuration 2: dyed photoresist over Si; (b) simulation of exposure with parameters in Table 2: isoexposure contours with 100-, 150-, and 300-J/cm³ levels.
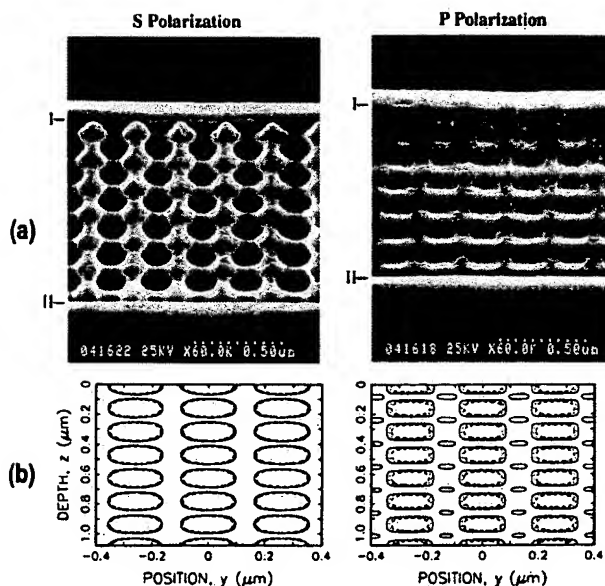

Fig. 7. (a) SEM results for configuration 3: addition of an oxide layer under the photoresist; (b) simulation at exposure with the parameters in Table 2: isoexposure contours with 20-, 25-, and 30-J/cm³ levels.

Configuration 2 examines the absorption effect with use of the dyed photoresist. The slightly greater photoresist thickness of 1.25 μm is used to enhance absorption effects. Figure 6(a) shows the cross-sectional SEM views of s- and p-polarized cases. Figure 6(b) shows the exposure simulations. Again, the elliptical form of s is different from the more rectangular p image. Higher-order development effects appear minimal. Compared with Fig. 5, the rectangular behavior of the p-polarized case is diminished, which is due to a reduction of the reflected z component at interface II. The absorption causes exposure to be strongest near interface I. This is confirmed in the SEM results by the reduction of standing-wave nodes near interface I. At this exposure, z-axis modulation of the interference minima is faintly visible in the p-polarization SEM.

Configuration 3 examines the distributions when an oxide layer is used under the photoresist. Commercial silicon wafers with evaporated SiO_2 were obtained with a measured index of $1.467 - 0.001i$ on a spectral ellipsometer. Using a regression analysis routine, internal to the ellipsometer unit, we determined that the oxide interface with Si was rough. Undyed photoresist was spun over the oxide. Figure 7(a) shows the SEM results for 30-s exposures. The effect of the SiO_2 is an axial shifting of the standing waves, as evidenced by an approximate standing-wave antinode close to interface II. Figure 7(b) shows this with the simulation results. The simulation shows a shift difference of ~200 Å when compared with the experiment. This is probably due to the rough oxide/Si interface, which is not modeled in the studies. The experimental images show the elliptical and rectangular behavior associated with configurations 1 and 2.

Configuration 4 attempts to minimize reflections from the Si substrate by using a dyed photoresist and an amorphous carbon underlayer. It is based on the calculations for minimizing r_{II} the reflectivity coefficient for interface II. Although a C layer of 600 Å is desired, a film of 525 Å was obtained, which is well within the region of the reflectivity minima. Figure 8(a) shows the SEM results with reduced standing-
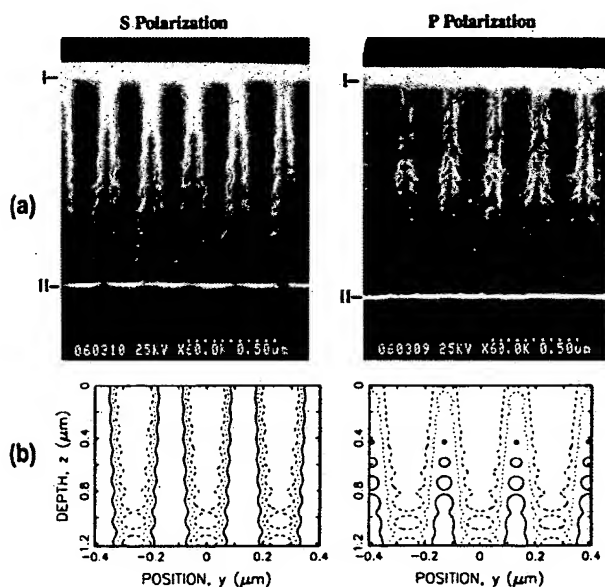

Fig. 8. (a) SEM results for configuration 4: dyed photoresist over C over Si; (b) simulation of exposure for the parameters in Table 2: isoexposure contours with 100-, 150-, and 200-J/cm³ levels.
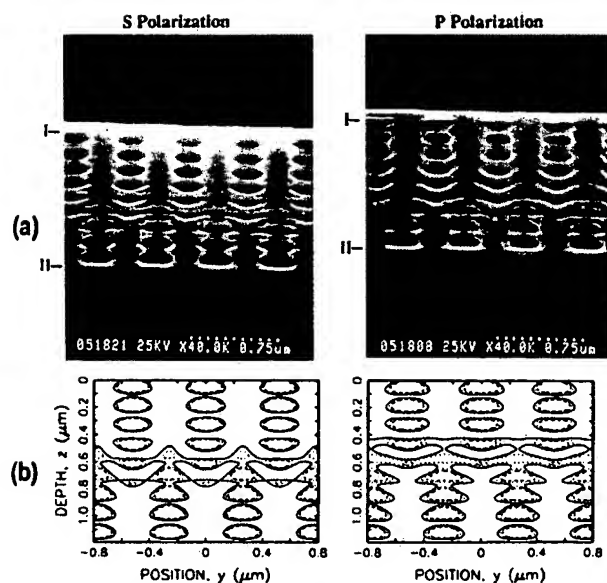
Fig. 9. (a) SEM results for configuration 5: undyed photoresist over Si; (b) simulation of exposure with $z_0 = 0$ and parameters in Table 2: isoexposure contours with 20-, 25-, and 30-J/cm^3 levels.

wave patterns. The observation agrees with the simulations shown in Fig. 8(b). The change in line width from interface I to interface II is more apparent with this experiment. The elliptical and rectangular behavior is absent from experimental and simulated structures, which is due to minimized reflectance at interface II. The p-polarization image exhibits low contrast, as evidenced by the absence of sharp edges. This low contrast is due to relatively
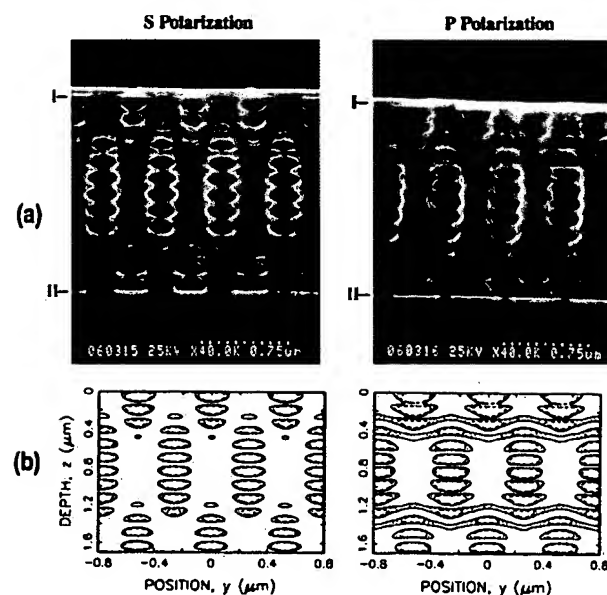

Fig. 10. (a) SEM results for configuration 6: undyed photoresist over Si with $z_0 = 0$; (b) simulation of exposure for the parameters in Table 2: isoexposure contours with 20-, 25-, and 30-J/cm^3 levels.
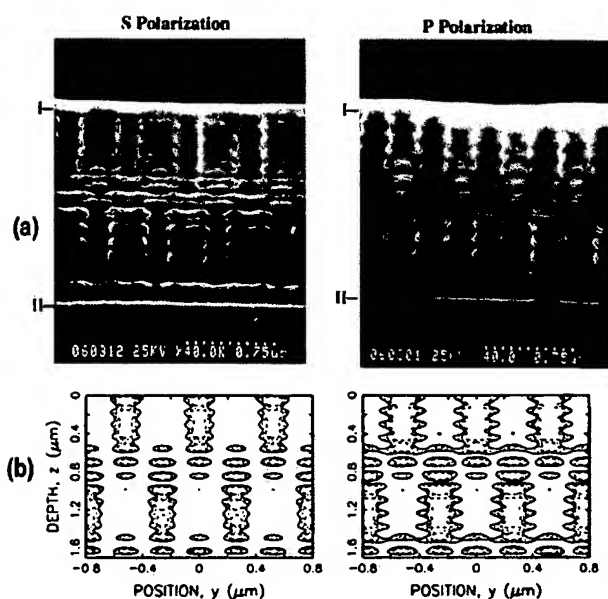

Fig. 11. (a) SEM results for configuration 6: undyed photoresist over Si, $z_0 = 0.8$ µm; (b) simulation of exposure for the parameters in Table 2: isoexposure contours with 20-, 25-, and 30-J/cm^3 levels.

large background exposure levels that are also observed in the simulations.

The objective of the three-beam studies is to determine the effects of the central order. The same setup is used as in the two-beam experiment, except the 0th order is allowed to interfere with the ±1st orders for s- and p-polarization conditions. The focus offset z_0, which is absent from the two-beam experiments, is significant with three-beam interference.

Configuration 5 uses unattenuated orders from the grating, such that the ±1st orders have approximately 36% power of the 0th order. Figure 9(a) shows the SEM views and Fig. 9(b) shows the simulations. The effects of focus through the film are clearly evident by the image structure inverting itself between interface I and interface II. The simulations in Fig. 9(b) show small differences between s and p, which are mainly associated with the midpoint of the film. There is slightly more background power in the p image and no substantial difference in shape between standing-wave maxima. This is due to the strong central order that dominates over the weaker oblique orders. The SEM photographs in Fig. 9(a) show verification of the focus behavior but no significant polarization differences. Differences between simulation and experiment are due to the choice of exposure time, which places the average exposure energy at approximately the photoresist speed point.

The objective of configuration 6 is to determine the effect of polarization when each of the ±1st orders have the same power as the 0th order. A neutral density filter is used to attenuate the 0th order such that its irradiance is equivalent to each of the ±1st orders. Figure 10(a) shows the SEM view for an estimated focus offset of $z_0 = 0$, and Fig. 10(b) shows

the simulations. The photoresist thickness has been increased to 1.7 μm to highlight focusing effects. The s- and p-polarizations simulations show slight differences. There is some squaring of the edges with the maxima in the p image that does not occur with s. Because the power of the central order has been reduced, the relative contribution of the oblique orders has increased. Hence our experiments are recording the onset of the rectangular maxima observed with two-beam interference. The SEM photographs show some verification of these polarization features. They also show good agreement with the inversion of the pattern through the depth of the photoresist.

Figure 11(a) shows SEM views for an estimated focus offset of $z_0 = 0.8$. The simulations are displayed in Fig. 11(b). Again, verification can be clearly seen with the pattern inversion. The photographs show slight differences between s and p. The p image contains wider exposed regions than s and less contrast.

5. Summary

We have compared two-beam and three-beam exposure models with experiments that use a unique decoration technique to examine cross sections of the image within the photoresist. The use of a photoresist as a detector of the image record is explained through a simple photoresist development model that approximates the photoresist behavior. In all cases, the exposure model accurately predicts feature characteristics.

Two-beam interference experiments with plane waves at 0.85 NA show strong differences between the s- and p-polarized illumination. Experiments that use reflective underlayers show that s polarization produces elliptical features whereas p polarization yields rectangular features. These features depend on the reflectivity of the z component. Our experiments demonstrate the reduction of these features by minimizing the substrate reflectivity. A

dyed photoresist or an antireflective layer between the photoresist and the substrate can be used to minimize reflection. With a dyed photoresist and an antireflection layer, the contrast is lower with p polarization because of relatively high background levels.

Three-beam interference experiments show that the vector effects that are present in the two-beam configuration are diminished. The polarization effects, which are due to the obliquity of the ±1st orders, are greatly reduced by the addition of a strong zero order. These effects increase as the relative power of the zero order is diminished. The effects of focus through the film are observed as an image inversion from the top surface to the bottom of the film. p-polarized illumination produces lower contrast images.

References

1. G. Owen, R. F. W. Pease, D. A. Markle, A. Grenville, R. L. Hsieh, R. von Bünau, and N. I. Mauluf, "1/8 μm optical lithography," J. Vac. Sci. Technol. B 10, 3032–3036 (1992).
2. D. G. Flagello and A. E. Rosenbluth, "Vector diffraction analysis of phase-mask imaging in photoresist films," in Optical/Laser Microlithography, J. D. Cuthbert, ed., Proc. SPIE 1927, 395–412 (1993).
3. D. G. Flagello, T. Milster, and A. E. Rosenbluth, "Theory of high-NA imaging in homogeneous thin films," J. Opt. Soc. Am. A 13, 53–64 (1996).
4. D. G. Flagello, "High numerical aperture imaging in homogeneous thin films," Ph.D. dissertation (University of Arizona, Tucson, Ariz., 1993).
5. Y. Uetani, M. Hanabata, and A. Furuta, "Observation of internal structure of a positive photoresist image using cross-sectional exposure method," J. Vac. Sci. Technol. B 7, 569–571 (1989).
6. D. C. LaTulipe, A. T. S. Pomerene, J. P. Simmons, and D. E. Seeger, "Positive mode silylation process characterization," Microelectron. Eng. 17, 265–268 (1992).